



Design, hydrothermal synthesis and electrochemical properties of porous birnessite-type manganese dioxide nanosheets on graphene as a hybrid material for supercapacitors

Ying Liu^a, De Yan^{a,*}, Renfu Zhuo^a, Shuankui Li^a, Zhiguo Wu^a, Jun Wang^a, Pingyuan Ren^a, Pengxun Yan^{a,b}, Zhongrong Geng^c

^a School of Physical Science and Technology, Lanzhou University, Lanzhou 730000, People's Republic of China

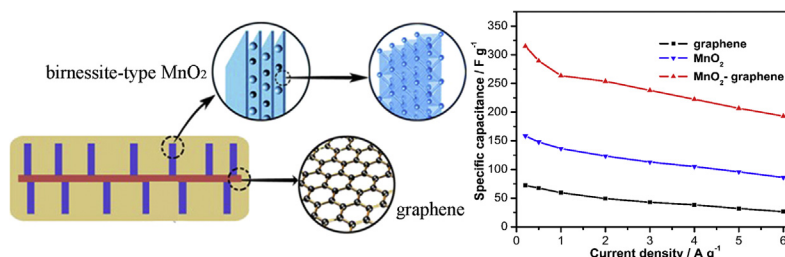
^b Key Laboratory of Solid Lubrication, Institute of Chemistry and Physics, Chinese Academy of Science, Lanzhou 730000, People's Republic of China

^c School of Mechatronic Engineering, Lanzhou Jiaotong University, Lanzhou 730070, People's Republic of China

HIGHLIGHTS

- A MnO₂–graphene hybrid has been designed and synthesized.
- Porous birnessite-type MnO₂ nanosheets grown on graphene sheets.
- MnO₂–graphene electrode exhibits excellent electrochemical performances.
- The superior capacitive performance is attributed to its unique structure.

GRAPHICAL ABSTRACT



ARTICLE INFO

Article history:

Received 11 March 2013

Received in revised form

7 May 2013

Accepted 11 May 2013

Available online 25 May 2013

Keywords:

Birnessite-type manganese dioxide

Graphene

Hydrothermal method

Supercapacitors

ABSTRACT

MnO₂–graphene hybrid with a unique structure of porous birnessite-type manganese dioxide (MnO₂) nanosheets on graphene has been designed and synthesized by a simple hydrothermal method. The formation mechanism of the hybrid is discussed based on a series of time-dependent experiments. Electrochemical measurements reveal that the MnO₂–graphene electrode exhibits much higher specific capacitance (315 F g^{−1} at a current density of 0.2 A g^{−1}) and better rate capability (even 193 F g^{−1} at 6 A g^{−1}) compared with both the graphene and MnO₂ electrodes. Moreover, the capacitance of MnO₂–graphene electrode is still 87% retained after 2000 cycles at a charging rate of 3 A g^{−1}. The superior capacitive performance of the hybrid is attributed to its unique structure, which provides good electronic conductivity, fast electron and ion transport, and high utilization of MnO₂.

© 2013 Elsevier B.V. All rights reserved.

1. Introduction

In the last few years there has been great research in flexible energy-storage systems, which can find applications in various fields, including electric vehicles, consumer electronics, memory

back-up systems, industrial power, energy management, and military devices. Supercapacitors, with the advantages of high power density, rapid charging–discharging rates, long cycle life, and good operational safety, are considered to be one of the most-promising energy-conversion and storage systems to fulfill future energy-storage needs [1,2].

Various materials, such as carbonaceous materials [3–7], conducting polymers [8,9] and transition-metal oxides [10–12] have been investigated as the electrode material for supercapacitors.

* Corresponding author. Tel.: +86 931 8912719; fax: +86 931 8913554.

E-mail addresses: yand@lzu.edu.cn, 332750098@163.com (D. Yan).

Amongst all these materials, MnO_2 is believed to be a promising supercapacitive material for the next generation of supercapacitors because of its low cost, environmental benignity, and excellent capacitive performance in aqueous electrolytes [13–16]. However, the reported specific capacitance values of the MnO_2 electrodes are still far below the theoretical value (approximately 1370 F g^{-1}), which are attributed to the intrinsically poor electronic conductivity of MnO_2 [17].

Recently, intensive studies have focused on hybrid materials, which incorporate MnO_2 nanosheets on high-surface-area conductive support (e.g., carbon nanofoams, carbon nanotubes (CNTs), templated mesoporous carbon), to optimize the electrochemical performance of MnO_2 [18–22]. Graphene, the 2D form of carbon, has become a ‘rising star’ owing to its large specific surface area, extraordinarily high electrical and thermal conductivities, and superior mechanical strength [23,24]. It is conceived as extremely promising electrochemical double-layer (EDL) supercapacitor electrode material in consideration of its excellent electrochemical performance (135 F g^{-1}) over a wide range of voltage scan rates [25]. MnO_2 –graphene hybrids which combine the high specific capacitance of MnO_2 and good conductivity of graphene have exhibited remarkably improved electrochemical performance [26–32]. However, the structure of these hybrids should be rationally designed to ensure making the best use of each ingredient’s advantages and the synergetic effect between them. Structure designing is now becoming a great challenge to the development of graphene based hybrid materials for supercapacitors.

MnO_2 –graphene hybrid with a unique structure of porous birnessite-type MnO_2 nanosheets on graphene has been designed and the illustration of the structure is shown in Fig. 1. In this hybrid, graphene sheets mainly serve as highly conductive supports, which can provide large surfaces for the deposition of MnO_2 nanosheets. The excellent interfacial contact between MnO_2 and graphene can significantly improve the conductivity of electrode. On the other hand, the interconnected MnO_2 nanosheets have several advantages. Firstly, the porous morphology can greatly increase the contact area and surface accessibility between MnO_2 and electrolyte, thus promote the specific capacitance and the utilization of MnO_2 . Secondly, the thin sheets can shorten the diffusion path of electron and ions, accordingly improving the rate capability and cycle stability of the electrode. Thirdly, the interconnected nanosheets can effectively prevent MnO_2 from conglomeration. Obviously, this rationally designed hybrid not only can combine the each other’s advantages of MnO_2 and graphene, but also make the best use of the synergetic effect between them. Thus, it is expected to exhibit excellent electrochemical performances of high specific capacitance, good rate capability and long cycling life.

In this work, the designed MnO_2 –graphene hybrid material has been synthesized by a simple hydrothermal method. The structure, morphology, growth mechanism and excellent electrochemical properties of the hybrid are fully investigated and discussed. Moreover, the electrochemical properties of pristine graphene and MnO_2 nanoflakes were also investigated for comparison.

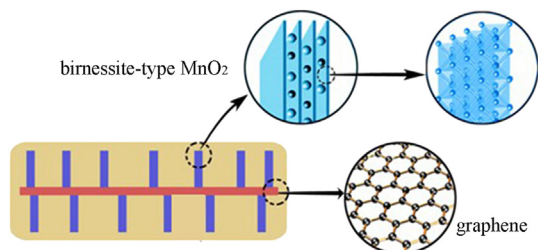


Fig. 1. Illustration represents the structure of MnO_2 –graphene hybrid.

2. Experimental section

2.1. Synthesis of reduced graphene oxide

Graphite oxide (GO) was bought from natural graphite (Nanjing XFNANO Company). The GO was suspended in water to give a brown dispersion, which was subjected to dialysis to completely remove residual salts and acids. The as-purified GO suspensions were dispersed in water to create 0.05 wt% dispersion. Exfoliation of GO was achieved by ultrasonication of the dispersion using an ultrasonic bath (KQ-600KDE, 600W). In a typical procedure for chemical conversion of GO to graphene, the resulting homogeneous dispersion (100 mL) was mixed with 100 mL of water, 2 mL of hydrazine solution (20 wt% in water, BASF) in a 250 mL round-bottom flask and the pH of the suspension was adjusted to 10 using sodium hydroxide solution (Tianjin Chemical Company), and then refluxed at 90°C for 24 h. Finally, the solid was washed with distilled water and dried at 80°C for 12 h in a vacuum oven.

2.2. Synthesis of MnO_2 –graphene hybrid

The MnO_2 –graphene hybrid was prepared by a hydrothermal method. In the first step, 10 mg graphene were dispersed in 30 mL deionized water by ultrasonic vibration for 15 min. Then potassium permanganate (KMnO_4) powder (30 mg) was added into above graphene suspension and stirred by magnetic bar for 5 min. After that, the mixed solution was transferred to a 40 mL Teflon-lined stainless steel autoclave. The autoclave was sealed and put in an electric oven at 100°C for 6 h and then cooled to room temperature naturally. The black resultants were washed with distilled water and dried at 80°C for 12 h in a vacuum oven. The mass ratio of MnO_2 /graphene in the hybrid is 8.9:1, which is obtained from thermogravimetric analysis (see Supporting information I).

2.3. Synthesis of MnO_2 nanoflakes

For the preparation of birnessite-type MnO_2 nanoflakes, 30 mg KMnO_4 were placed into 30 mL DI water to form the precursor. The precursor solution was then treated with a hydrothermal reaction in a 40 mL Teflon-lined stainless steel autoclave at 120°C for 48 h. The resulted brownish black materials were rinsed with deionized water and dried at 80°C for 12 h in a vacuum oven.

2.4. Characterization methods

The crystallographic information of the products was investigated by X-ray diffraction (XRD, Shimadzu X-ray diffractometer 6000, Cu K α radiation) with a scan rate of $10^\circ \text{ min}^{-1}$. Raman spectra were measured on a Laser Raman spectroscopy (HORIBA Jobin Yvon LabRAM HR800) with 532 nm line of an Ar ion laser as an excitation source. Morphologies of the graphene, MnO_2 powder and MnO_2 –graphene hybrid were characterized by field emission scanning electron microscopy (FESEM, Hitachi S4800). The morphology and structure of the MnO_2 –graphene hybrid were further investigated by transmission electron microscopy (TEM, Tecnai-G2-F30). Thermogravimetric analysis (TGA) data were collected on a thermal analysis instrument (Setarm TGDTA92A) with a heating rate of 5°C min^{-1} in an air flow.

2.5. Preparation of electrodes

The fabrication of working electrode was carried out as follows. Briefly, the as-synthesized material (graphene sheets, MnO_2 nanoflakes or MnO_2 –graphene hybrid), carbon black and poly tetra fluoro ethylene (PTFE) were mixed in a mass ratio of 80:15:5 and

dispersed in ethanol. Then the resulting mixture was coated onto the nickel foam substrate (1 cm × 1 cm) with a spatula, which was followed by drying at 90 °C for 12 h in a vacuum oven. The loading mass of each electrode was about 6 mg.

2.6. Electrochemical measurements

To investigate the electrochemical behavior of the samples, cyclic voltammetry (CV) and galvanostatic charge/discharge (GCD) experiments were performed in a three-electrode mode using the as-prepared electrodes, a Pt foil and an Ag/AgCl (KCl saturated) electrode as the working electrode, the counter electrode and the reference electrode, respectively. All of the experiments were carried out on an electrochemical workstation (RST 5200) with 1 M Na₂SO₄ solution as the electrolyte at room temperature. CV tests were respectively done between 0 and 1.0 (vs. SCE) at different scan rates of 10, 20, 50, and 100 mV s⁻¹. GCD curves were measured in the potential range of 0–1.0 V (vs. SCE) at different current densities of 0.2, 0.5, 1, 2, 3, 4, 5, and 6 A g⁻¹, and electrochemical impedance spectroscopy (EIS) measurements were carried out in the frequency range from 100 kHz to 0.01 Hz at open circuit potential with an ac perturbation of 10 mV. According to the GCD curves, the specific capacitances of the electrodes were respectively calculated using the following equation:

$$C = (I\Delta t)/(\Delta V) \quad (1)$$

where C (F g⁻¹) is the specific capacitance, I (mA) is charge–discharge current, Δt (s) is the discharge time, m (mg) represents the loading mass of electroactive material, and ΔV (V) is the potential drop in the galvanostatic discharge process.

3. Results and discussion

3.1. Microstructure characterizations

Fig. 2 shows the XRD patterns of graphene, MnO₂, and MnO₂–graphene hybrid. As shown in Fig. 2a, graphene shows two diffraction peaks at 21.8° and 42.4°, which can be indexed as the (002) and (100) reflections of graphite, respectively [23]. The XRD pattern of the MnO₂ powder (Fig. 2b) synthesized by hydrothermal reaction can be indexed to the monoclinic potassium birnessite (JCPDS NO.86-0666), which consists of 2-D, edge-shared [MnO₆] octahedral layers with K⁺ cations and water molecules in the interlayer space. The four diffraction peaks at 12.3°, 24.8°, 36.6° and 65.5° correspond to (003), (006), (101) and (110) basal reflections, respectively [33]. From the XRD pattern of the MnO₂–graphene

hybrid (Fig. 2c), diffraction peaks from the birnessite-type MnO₂ phase can be observed but the diffraction peaks from the graphene can hardly be seen, indicating a high mass loading of MnO₂.

To further confirm the existence of graphene in the MnO₂–graphene hybrid material, these samples were also investigated by Raman scattering, as shown in Fig. 3. For the Raman spectrum of the pristine graphene (Fig. 3a), the G band (1601 cm⁻¹) represents the in-plane bond-stretching motion of the pairs of C sp² atoms (the E_{2g} phonons), while the D band (1360.5 cm⁻¹) corresponds to breathing modes of rings or K-point phonons of A_{1g} symmetry [34,35]. As shown in Fig. 3b, the three Raman bands located at 495.7, 575.9 and 629.8 cm⁻¹ are in good accordance with the three major vibration features of the birnessite-type MnO₂ compounds previously reported at 490–510, 575–585, and 625–650 cm⁻¹ [19,36]. In Fig. 3c, three birnessite-type MnO₂ bands and two graphene bands can be clearly observed, indicating the existence of graphene in the hybrid.

The morphology of these samples was characterized by FESEM and TEM, as shown in Fig. 4. It can be seen that the agglomerated graphene prepared from reduction of graphene oxide are micro-sized sheets with thickness of about 5 nm (Fig. 4a), and the MnO₂ powder is composed of nanoflakes about 10 nm in thickness (Fig. 4b). FESEM images of the MnO₂–graphene hybrid (Fig. 4c and d) show that the MnO₂ layer is about 100 nm in thickness and consists of numerous interconnected tiny nanosheets which uniform and vertically grow on both side of the graphene surface. Seen from Fig. 4e, the MnO₂ nanosheets is about 3–5 nm in thickness. The inset in Fig. 4e shows the selected area electron diffraction (SAED) pattern of the hybrid, and the three diffraction rings are corresponding to the (003), (113) and (015) crystal planes of MnO₂. Fig. 4f shows the high resolution transmission electron microscopy (HRTEM) image of MnO₂ nanosheets and graphene substrate. It can be clearly seen that the MnO₂ nanosheets grow vertically on the surface of graphene. The interplanar spacing of MnO₂ nanoflake is 0.71 nm, which is the typical interplanar spacing of birnessite-type MnO₂ as reported in other literatures [37,38].

3.2. Formation mechanism

The formation mechanism of the hybrid was investigated by a series of time-dependent experiments. When the mixed solution of graphene suspension and KMnO₄ reacted under hydrothermal condition for 15 min, numerous MnO₂ nuclei uniformly grew on the graphene surface, as shown in Fig. 5a. In this nucleation stage, the remained oxygen-containing functionalities (epoxide, hydroxyl, carbonyl and carboxyl groups) on graphene surface are vulnerable to oxidation [39,40], and direct electron transfer from sheet defects

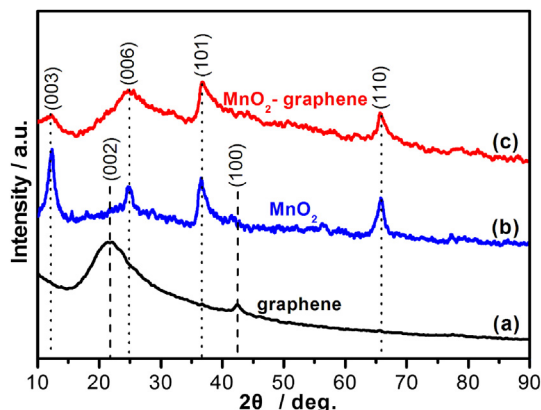


Fig. 2. XRD patterns of the (a) graphene, (b) MnO₂ and (c) MnO₂–graphene hybrid.

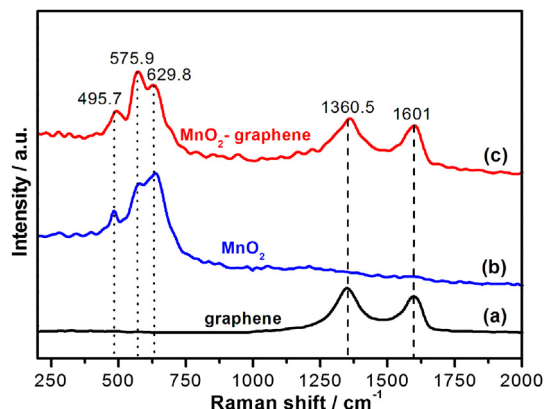


Fig. 3. Raman spectrum of the (a) graphene, (b) MnO₂ (c) MnO₂–graphene hybrid.

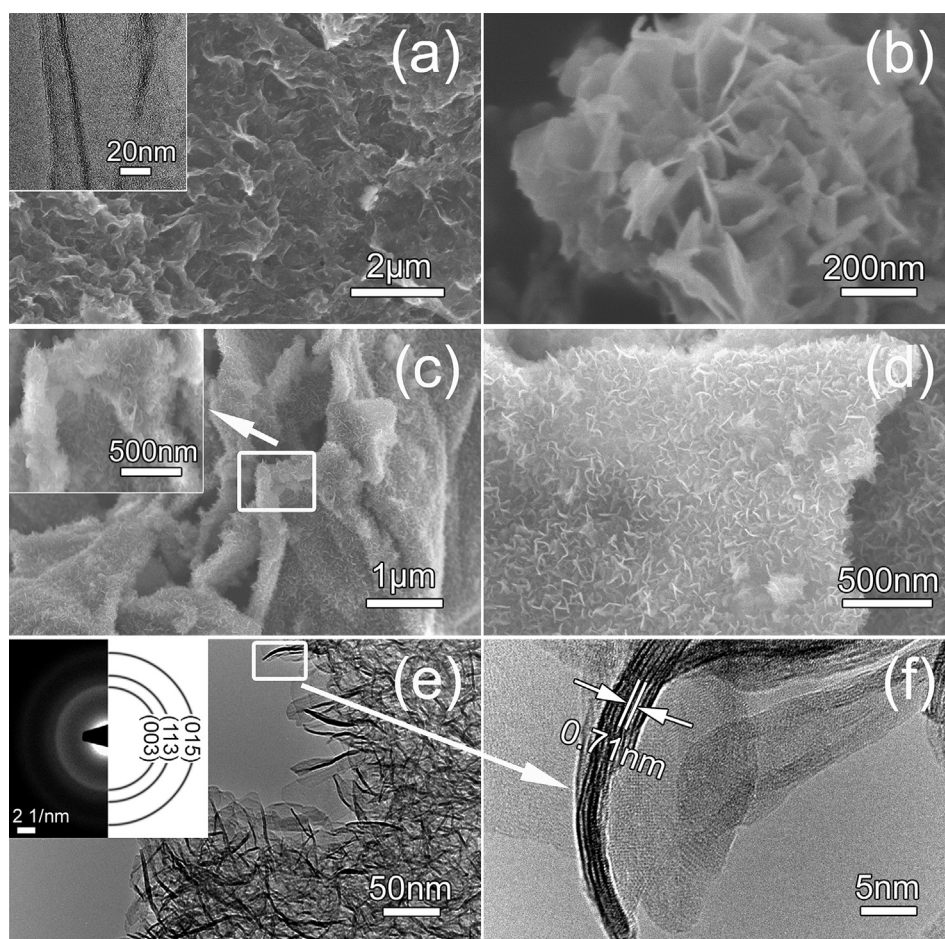


Fig. 4. FESEM and TEM images. FESEM images of the (a) graphene (the inset shows the TEM image of graphene sheets), (b) MnO_2 , (c) and (d) MnO_2 –graphene hybrid. (e) TEM image of the MnO_2 –graphene hybrid and corresponding SAED pattern. (f) HRTEM image of the MnO_2 –graphene hybrid.

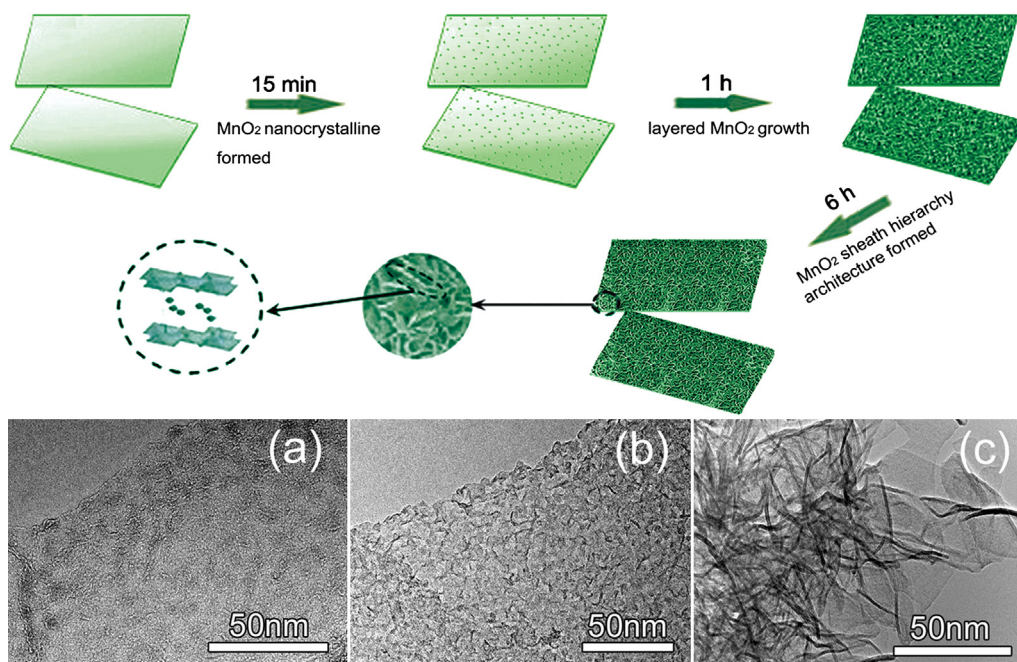
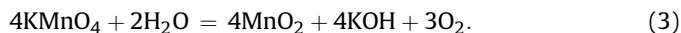
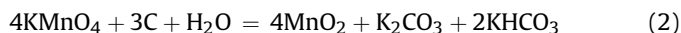


Fig. 5. Illustration represents the formation mechanism of MnO_2 –graphene hybrid and TEM images of the hybrids synthesized after different hydrothermal reaction time. (a) 15 min, (b) 1 h, and (c) 6 h.

to MnO_4^- results in easy MnO_2 precipitation near the defect sites. There are two reactions could lead to the precipitation of MnO_2 nucleus [41], which can be expressed by the follows equations:



The slow redox reaction (2) usually leads to the precipitation of MnO_2 nuclei on the surface of graphene, but it can not make the major contribution to the further growth of MnO_2 nanosheets on the graphene, because the self-limiting deposition of KMnO_4 in hydrothermal reaction (3) is much faster than the redox reaction between KMnO_4 and graphene [19,42]. Thus, the self-limiting deposition of KMnO_4 may be the dominant reaction in the whole hydrothermal process. With the reaction time increased to 1 h (Fig. 5b), the rudiments of MnO_2 nanosheets were formed, and then fully developed when the reaction time was prolonged to 6 h (Fig. 5c). In this growing stage, the MnO_2 molecules formed by reaction (3) slowly deposited on the nucleation sites and the pre-formed nanosheets grew along the ab plane, which is the preferred growth direction of layered birnessite-type MnO_2 under hydrothermal condition [33,41]. Consequently, the as-designed unique hybrid was obtained.

3.3. Electrochemical performances

CV curves of the graphene, MnO_2 , and MnO_2 -graphene electrodes in 1 M Na_2SO_4 electrolyte at different scan rates are shown in

Fig. 6. The CV curves of graphene electrode exhibit a little deviation from rectangular shape, indicating the presence of pseudo-capacitance. In contrast, the deviation from rectangularity of the CV curves for MnO_2 electrode becomes obvious as the scan rate increases, especially at a high scan rate of 100 mV s^{-1} . This can be ascribed to the change of ion transplanted surrounding, for which the ions can only reach the outer surface of the electrode and not enter into the interior pores at a large scan rate [5,16]. However, the current densities for MnO_2 electrode increase significantly compared with those of the graphene electrode, which indicate that the MnO_2 electrode can deliver a much higher capacitance. For the MnO_2 -graphene electrode, the CV curves still retain nearly rectangular shape even at 100 mV s^{-1} , presenting remarkably improved rate capability compared with the MnO_2 electrode. Moreover, the current densities of the MnO_2 -graphene electrode are much larger than those of the graphene and MnO_2 electrodes, suggesting a high specific capacitance and utilization of MnO_2 in the hybrid.

In order to investigate the capability of the materials, GCD tests of the graphene, MnO_2 , and MnO_2 -graphene electrodes were carried out at different constant current densities, as shown in Fig. 7. The GCD curves of the graphene electrode (Fig. 7a) show rapid charge–discharge rates and a little deviation from symmetrical variations of the voltage during the charging–discharging process. The deviations of the GCD curves are related to the quick Faradaic reactions, due to the presence of additional oxygen-containing functional groups, especially epoxy and alkoxy, at the surface of the chemical reduced graphene oxide [43]. However, linear variations of the potential are observed in the GCD curves of MnO_2

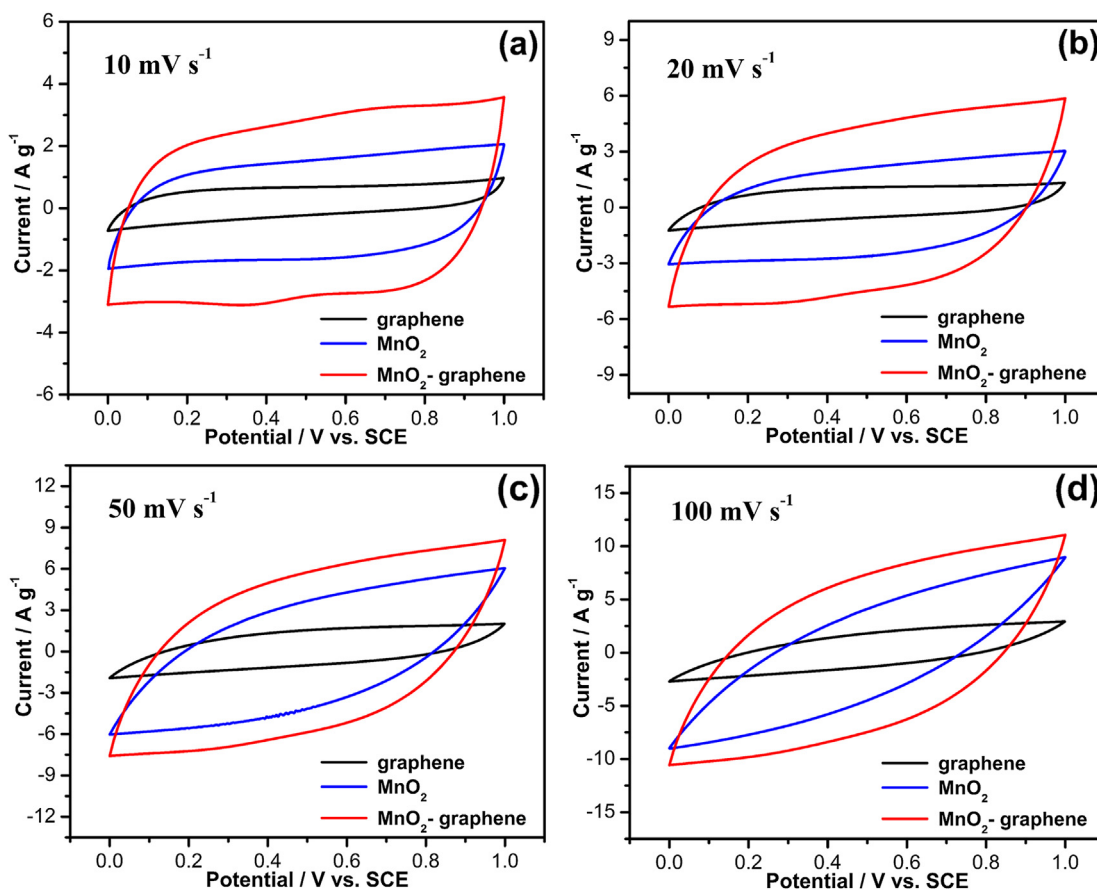


Fig. 6. CV curves of the graphene, MnO_2 and MnO_2 -graphene electrodes vs. different scan rates. (a) 10 mV s^{-1} , (b) 20 mV s^{-1} , (c) 50 mV s^{-1} , and (d) 100 mV s^{-1} .

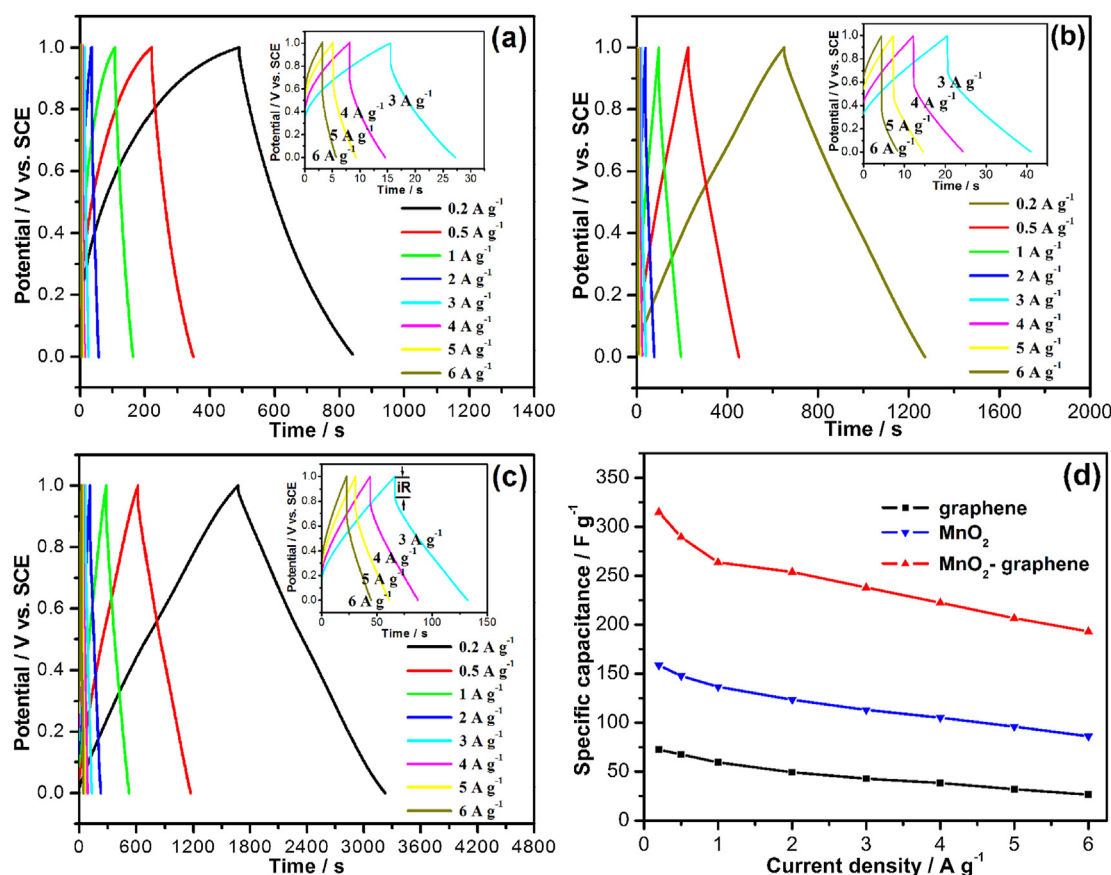


Fig. 7. GCD curves and specific capacitance of the electrodes vs. current densities from 0.2 to 6 A g⁻¹. GCD curves of the electrodes for (a) graphene, (b) MnO₂, and (c) MnO₂-graphene hybrid. (d) Specific capacitance for different electrode materials.

electrode (Fig. 7b), which could be ascribed to reversible redox transitions involving the exchange of protons and/or cations with the electrolyte, as well as the transitions between Mn(IV) and Mn(III) within the electrode potential window of the electrolyte [1,21]. As shown in Fig. 7c, the MnO₂-graphene electrode exhibit longer discharge time and highly symmetric triangular charge/discharge curves, confirming the hybrid has high specific capacitance, excellent reversibility and charge-discharge properties. Fig. 7d compares the specific capacitances at different constant current densities for the three electrodes. The capacitance of the graphene electrode decreases from 72 to 26 F g⁻¹ with the increased current density from 0.2 to 6 A g⁻¹. This can be explained by an increased internal polarization at higher current densities [44,45]. For the current density increased to 6 A g⁻¹, the *iR* drop is too large to permit an accurate calculation of the specific capacitance. The specific capacitance of MnO₂ electrode is 158, 146, 136, 123, 113, 105, 96 and 86 F g⁻¹ at current density of 0.2, 0.5, 1, 2, 3, 4, 5 and 6 A g⁻¹, respectively. In contrast, the MnO₂-graphene electrode exhibits specific capacity of 315, 289, 263, 253, 237, 222, 206 and 193 F g⁻¹ at 0.2, 0.5, 1, 2, 3, 4, 5 and 6 A g⁻¹, respectively. It is noteworthy that the specific capacitance is measured at a high mass loading of 6 mg cm⁻², which is much higher than that investigated in other recent reports on MnO₂-graphene electrodes [26,27,32].

The excellent superior capacitive behavior of the present MnO₂-graphene electrode is attributed to its unique characteristics. Firstly, each MnO₂ nanosheet grows directly on the graphene surface. The graphene construct a 3D highly conductive current collector which can significantly increase the electronic conductivity of the electrode. Secondly, the nanoscopic MnO₂ sheets not

only offer large electrochemically active surface area for charge transfer, but also reduce the solid-state transport distances for both ions and electrons into MnO₂ [18–20]. It ensures a good rate capability, a high specific capacitance, as well as a high utilization of the electrode materials. Thirdly, the highly porous structure of MnO₂ layer shortens the diffusion distance of electrolyte to the interior surfaces of MnO₂, which facilitates better penetration of the electrolyte into the electrode material and enhances the ionic conductivity of the electrode material [21,25]. With the unique nanostructure, the MnO₂-graphene electrode can display excellent electrochemical capacitive performances even at a high mass loading of electrode material.

The EIS analysis has been recognized as one of the principal methods for examining the fundamental behavior of electrode materials, which not only provides useful information on the electrochemical frequency of the system but also allows for the measurement of redox reaction resistance and equivalent series resistance of the electrode [46]. Impedance spectra of the graphene, MnO₂, and MnO₂-graphene electrodes are shown in Fig. 8. The Nyquist plots can be divided into three parts: (1) a high-frequency intercept, (2) a semicircle in the high-to-medium-frequency region, and (3) a straight line inclining about 45° to the real axis or an almost vertical line in the low frequency region. The high-frequency intercepts for all the three electrodes are almost the same, indicating that they have the same combinational resistance of ionic resistance of electrolyte, intrinsic resistance of substrate, and contact resistance at the active material/current collector interface (*R_c*). The semicircle in the high-to-medium-frequency region corresponds to a parallel combination of charge transfer

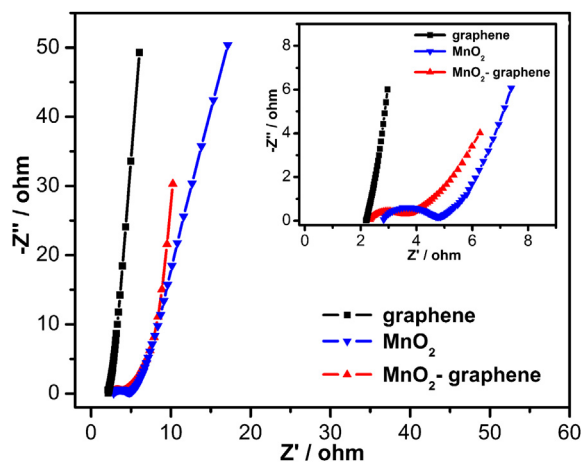


Fig. 8. Nyquist plots of the graphene, MnO_2 and MnO_2 -graphene electrodes.

resistance (R_{ct}) and the double-layer capacitance (C_{dl}) on the grain surface [26]. As the value of R_{ct} is equal to the diameter of the semicircle [19,46], the R_{ct} of the MnO_2 -graphene electrode is much smaller than that of the MnO_2 electrode. This owes to the unique structure of MnO_2 -graphene hybrid, which facilitates a faster cation insertion/extraction process into/from MnO_2 lattice [47,48]. For a simple electrode-electrolyte system, low-frequency straight line exhibits a slope of 45° if the process is under diffusion control, or a slope of 90° if the system is purely capacitive in nature [49,50]. The almost vertical line for the graphene electrode demonstrates a good capacitive behavior without diffusion limitation. The finite slope of low-frequency straight line represents the diffusive resistance of electrolyte in electrode pores or cation diffusion in the host materials [51]. It can be seen that the slope of the straight line for MnO_2 -graphene electrode is similar to that of the graphene electrode, but much larger than that of the MnO_2 electrode. This observation indicates that the MnO_2 -graphene electrode has much lower diffusive resistance compared with the MnO_2 electrode. Furthermore, the 45° sloped portion at the mid-frequency region is the typical Warburg resistance reflecting the ion diffusion behavior of the electrolyte. The smaller Warburg region, the lower electronic transport resistance, less obstruction for ion diffusion and better charge propagation behavior [25,46]. As shown in the inset of Fig. 8, the MnO_2 -graphene electrode has a smaller Warburg region, which presents a minor Warburg resistance. It implies that the highly porous MnO_2 nanosheets decorated on the surface of graphene is able to facilitate the penetration of electrolyte, leading to fast diffusion of electrolyte into the pores of MnO_2 . Thus, the unique structure of MnO_2 -graphene hybrid facilitates small charge transfer resistance, diffusive resistance and Warburg resistance, which can make for fast electron and ion transport. Thus, the MnO_2 -graphene electrode could show good charge propagation behavior and ideal supercapacitive performance.

The cycle stability of the MnO_2 -graphene hybrid was evaluated by repeating the GCD test in the potential range of 0–1.0 V (vs. SCE) at a current density of 3 A g^{-1} for 2000 cycles. The capacitance retention ratio as a function of cycle number is presented in Fig. 9a. After 2000 cycles, the capacitance still remained 87% of the initial capacitance, demonstrating good electrochemical stability of the synthesized MnO_2 -graphene hybrid.

To further evaluate the electrochemical behavior of the MnO_2 -graphene electrode before and after the cycle tests, EIS analyses after the 1st and 2000th cycles were measured (as shown in Fig. 9b). Both the impedance spectra are almost the same profile and consist of similar patterns such as a high-frequency intercept, a

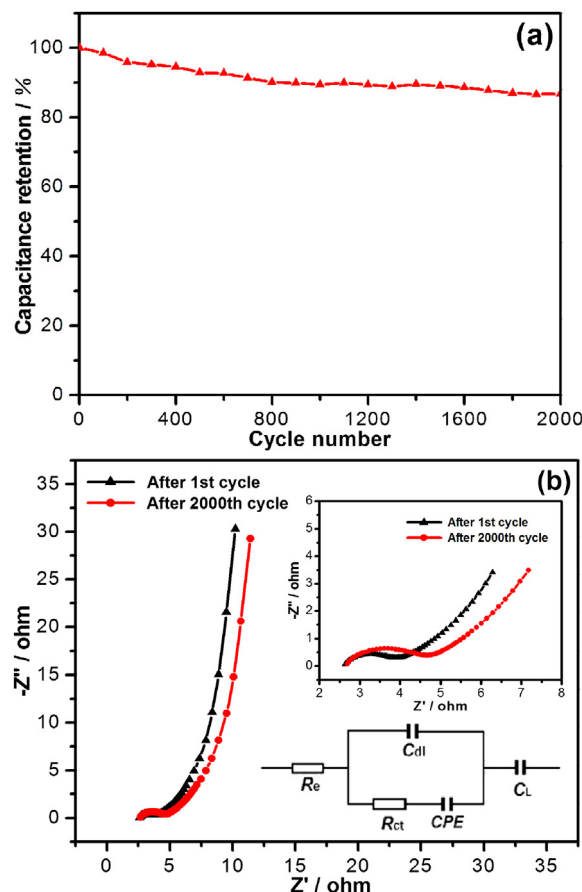


Fig. 9. (a) Variation of the specific capacitance of MnO_2 -graphene electrode as a function of cycle number measured at 3 A g^{-1} . (b) Nyquist plots of MnO_2 -graphene electrode in the frequency range of 100 kHz to 0.01 Hz, the inset is the electrical equivalent circuit used for fitting impedance spectra.

semicircle in the high-to-medium-frequency region, a straight line inclining about 45° to the real axis in the mid-frequency region, and an almost vertical line in the low frequency region. The major difference is that a larger semicircle diameter arises in the Nyquist plot of MnO_2 -graphene electrode after 2000th cycles. The measured impedance spectra were analyzed using the complex nonlinear least-squares (CNLS) fitting method on the basis of the equivalent circuit [46,47], which is given in the inset of Fig. 9b. Where the CPE is the constant phase angle element relates to the Warburg resistance [52], and C_L is the limit capacitance [53,54]. The obtained values of R_e , C_{dl} , R_{ct} , CPE and C_L were calculated from CNLS fitting of the experimental impedance spectra and presented in Table 1. After 2000 cycles, the calculated R_{ct} increases from 7.908 to 12.51 Ω , while the value of C_{dl} decreases from 231.1 to 194.6 μF . It is probably resulted from the loss of adhesion of some active material with the current collector or the dissolution of MnO_2 during the charge/discharge cycling [26,55]. Furthermore, the decreased CPE is attributed to the decreased diffusion and migration pathways of electrolyte ions during the charge/discharge processes [48].

Table 1

The calculated values of R_e , C_{dl} , R_{ct} , CPE and C_L through CNLS fitting of the experimental impedance spectra based upon the proposed equivalent circuit in Fig. 9b.

	R_e (Ω)	C_{dl} (μF)	R_{ct} (Ω)	CPE ($\Omega^{-1}\text{s}^{1/2}$)	C_L (F)
1st cycle	2.848	231.1	7.908	0.3232	0.6221
2000th cycle	2.85	194.6	12.51	0.2847	0.6386

4. Conclusions

MnO₂–graphene hybrid with a unique structure of porous Bir-MnO₂ nanosheets on graphene surfaces has been designed and synthesized by a simple hydrothermal treatment. The formation mechanism of the hybrid synthesized by the self-limiting deposition of KMnO₄ under hydrothermal reaction is discussed. Electrochemical measurements reveal that the MnO₂–graphene electrode exhibits much higher specific capacitance and better rate capability compared with both the graphene and MnO₂ electrodes. Specifically, the MnO₂–graphene electrode displays a high specific capacitance of 315 F g^{−1} at current density of 0.2 A g^{−1}, good capability with a capacitance of 193 F g^{−1} even at 6 A g^{−1}, as well as excellent cycle stability with capacitance retention of 87% at 3 A g^{−1} after 2000 cycles, indicating a promising potential application as an effective candidate for supercapacitors. The superior capacitive performance of MnO₂–graphene hybrid is attributed to its unique structure, which provides good electronic conductivity, fast electron and ion transport, and high utilization of MnO₂.

Acknowledgments

This work is supported by the National Natural Science Foundation of China (Grant No. 11204114, Grant No. 11004098 and Grant No. 11104126) and the Fundamental Research Funds for the Central Universities (No. lzujbky-2012-29).

Appendix A. Supplementary material

Supplementary material related to this article can be found at <http://dx.doi.org/10.1016/j.jpowsour.2013.05.062>.

References

- [1] J.R. Miller, P. Simon, *Science* 321 (2008) 651–652.
- [2] C. Liu, F. Li, L.P. Ma, *Adv. Mater.* 22 (2010) E28–E62.
- [3] P. Simon, Y. Gogotsi, *Nat. Mater.* 7 (2008) 845–854.
- [4] L.L. Zhang, X.S. Zhao, *Chem. Soc. Rev.* 38 (2009) 2520–2531.
- [5] D. Pech, M. Brunet, H. Durou, P.H. Huang, V. Mochalin, Y. Gogotsi, P.L. Taberna, P. Simon, *Nat. Nanotechnol.* 5 (2010) 651–654.
- [6] M. Seredych, D. Hulicova-Jurcakova, G.Q. Lu, T.J. Bandoz, *Carbon* 46 (2008) 1475–1488.
- [7] M. Kaempgen, C.K. Chan, J. Ma, Y. Cui, G. Gruner, *Nano Lett.* 9 (2009) 1872–1876.
- [8] C.P. Fonseca, J.E. Benedetti, P. Neves, *J. Power Sources* 158 (2006) 789–794.
- [9] H.L. Wang, Q.L. Hao, X.J. Yan, L.D. Lu, X. Wang, *Electrochem. Commun.* 11 (2009) 1158–1161.
- [10] J.P. Liu, J. Jiang, C.W. Cheng, H.X. Li, J.X. Zhang, H. Gong, H.J. Fan, *Adv. Mater.* 23 (2011) 2076–2081.
- [11] C.C. Hu, K.H. Chang, M.C. Lin, Y.T. Wu, *Nano Lett.* 6 (2006) 2690–2695.
- [12] G. Wee, H.Z. Soh, Y.L. Cheah, S.G. Mhaisalkar, M. Srinivasan, *J. Mater. Chem.* 20 (2010) 6720–6725.
- [13] J. Yan, T. Wei, J. Cheng, Z.J. Fan, M.L. Zhang, *Mater. Res. Bull.* 45 (2010) 210–215.
- [14] W.F. Wei, X.W. Cui, W.X. Chen, D.G. Ivey, *Chem. Soc. Rev.* 40 (2011) 1679–1721.
- [15] A. Crossa, A. Morel, A. Cormiea, T. Hollenkamp, S. Donnea, *J. Power Sources* 196 (2011) 7847–7853.
- [16] X.Y. Lang, A. Hirata, T. Fujita, M.W. Cheng, *Nat. Nanotechnol.* 6 (2011) 232–236.
- [17] M. Toupin, T. Brousse, D. Belanger, *Chem. Mater.* 16 (2004) 3184–3190.
- [18] Y.T. Peng, Z. Chen, J. Wen, Q.F. Xiao, D. Weng, S.Y. He, H.B. Geng, Y.F. Lu, *Nano Res.* 4 (2011) 216–225.
- [19] H. Xia, Y. Wang, L.Y. Li, L. Lu, *Nanoscale Res. Lett.* 7 (2012) 1–10.
- [20] H.J. Zheng, J.X. Wang, Y. Jia, C.A. Ma, *J. Power Sources* 216 (2012) 508–514.
- [21] G.P. Wang, L. Zhang, J.J. Zhang, *Chem. Soc. Rev.* 41 (2011) 797–828.
- [22] Y. Zhang, H. Feng, X.B. Wu, L.Z. Wang, A.Q. Zhang, T.C. Xia, H.C. Dong, X.F. Li, L.S. Zhang, *Int. J. Hydrogen Energy* 34 (2009) 4889–4899.
- [23] Y.W. Zhu, S. Murali, W.W. Cai, X.S. Li, J.R. Potts, R.S. Ruoff, *Adv. Mater.* 22 (2010) 3906–3924.
- [24] P. Avouris, *Nano Lett.* 10 (2010) 4285–4294.
- [25] L.L. Zhang, R. Zhou, X.S. Zhao, *J. Mater. Chem.* 20 (2010) 5983–5992.
- [26] J. Yan, Z.J. Fan, T. Wei, W.Z. Qian, M.L. Zhang, F. Wei, *Carbon* 48 (2010) 3825–3833.
- [27] L. Mao, K. Zhang, H.S.O. Chan, J.S. Wu, *J. Mater. Chem.* 22 (2012) 80–85.
- [28] Y. Qian, S.B. Lu, F.L. Gao, *J. Mater. Sci.* 46 (2011) 3517–3522.
- [29] H.J. Huang, X. Wang, *Nanoscale* 3 (2011) 3185–3191.
- [30] Q. Cheng, J. Tang, J. Ma, H. Zhang, N. Shinya, L.C. Qin, *Carbon* 49 (2011) 2917–2925.
- [31] Z.P. Li, Y.H. Liu, X.H. Liu, S. Liu, S.R. Yang, J.Q. Wang, *J. Mater. Chem.* 21 (2011) 14706–14711.
- [32] H. Lee, J. Kang, M.S. Cho, M.S. Chio, Y.K. Lee, *J. Mater. Chem.* 21 (2011) 18215–18219.
- [33] D. Yan, P.X. Yan, S. Cheng, J.T. Chen, R.F. Zhou, J.J. Feng, G.A. Zhang, *Cryst. Growth Des.* 9 (2009) 218–222.
- [34] A.C. Ferrari, J. Robertson, *Phil. Trans. R. Soc. A* 362 (2004) 2477–2512.
- [35] L.G. Cancado, M.A. Pimenta, B.R.A. Neves, M.S. Dantas, A. Jorio, *Phys. Rev. Lett.* 9 (2004) 247401.
- [36] A. Ogata, S. Komaba, R. Baddour-Hadjean, J.P. Pereira-Ramos, N. Kumagai, *Electrochim. Acta* 53 (2008) 3084–3093.
- [37] Z.P. Liu, R.Z. Ma, Y. Ebina, K. Takada, T. Sasaki, *Chem. Mater.* 19 (2007) 6504–6512.
- [38] H.T. Zhu, J. Lou, H.X. Yang, J.K. Liang, G.H. Rao, J.B. Li, Z.M. Du, *J. Phys. Chem. C* 112 (2008) 17089–17094.
- [39] S. Stankovich, D.A. Dikin, R.D. Piner, K.A. Kohlhaas, A. Kleinhammers, Y.Y. Jia, W. Yue, S.B.T. Nguyen, R.S. Ruoff, *Carbon* 45 (2007) 1558–1565.
- [40] W. Gao, L.B. Alemany, L. Ci, P.M. Ajayan, *Nat. Chem.* 1 (2009) 403–408.
- [41] Z.P. Li, J.Q. Wang, Z.F. Wang, H.Q. Ran, Y. Li, X.X. Han, S.R. Yang, *New J. Chem.* 36 (2012) 1490–1495.
- [42] X.B. Jin, W.Z. Zhou, S.W. Zhang, G.Z. Chen, *Small* 3 (2007) 1513–1517.
- [43] B. Xu, S.F. Yue, Z.Y. Sui, X.T. Zhang, S.S. Hou, G.P. Cao, Y.S. Yang, *Energy Environ. Sci.* 4 (2011) 2826–2830.
- [44] J.J. Niu, W.G. Pell, B.E. Conway, *J. Power Sources* 156 (2006) 725–740.
- [45] H.Y. Mi, X.G. Zhang, X.G. Ye, S.D. Yang, *J. Power Sources* 176 (2008) 403–409.
- [46] B.E. Conway, *Electrochemical Supercapacitors: Scientific Fundamentals and Technological Applications*, Kluwer Academic/Plenum Press, New York, 1999, pp. 444–482.
- [47] W. Sugimoto, H. Iwata, K. Yokoshima, Y. Murakami, Y. Takasu, *J. Phys. Chem. B* 109 (2005) 7330–7338.
- [48] G.H. Yu, L.B. Hu, M. Vosgueritchian, H.L. Wang, X. Xie, J.R.M. Donough, X. Cui, Y. Cui, Z.A. Bao, *Nano Lett.* 11 (2011) 2905–2911.
- [49] P.L. Taberna, P. Simon, J.F. Fauvarque, *J. Electrochem. Soc.* 150 (2003) A292–A300.
- [50] S. Devaraj, N. Munichandraiah, *J. Electrochem. Soc.* 154 (2007) A80–A88.
- [51] M.W. Xu, L.B. Kong, W.J. Zhou, H.L. Li, *J. Phys. Chem. C* 111 (2007) 19141–19147.
- [52] M.D. Stoller, S.J. Park, Y.W. Zhu, J.H. An, R.S. Ruoff, *Nano Lett.* 8 (2008) 3498–3502.
- [53] A.D. Fabio, A. Giorgi, M. Mastragostino, F. Soavi, *J. Electrochem. Soc.* 186 (2001) A850–A854.
- [54] M.S. Wu, C.Y. Huang, K.H. Lin, *J. Power Sources* 186 (2009) 557–564.
- [55] S.R. Sivakumar, J.M. Ko, D.Y. Kim, B.C. Kim, G.G. Wallace, *Electrochim. Acta* 52 (2007) 7377–7385.